nature communications

Article

https://doi.org/10.1038/s41467-026-68604-z

Operando nuclear magnetic resonance decodes alkali-tuned proton-electron relay boosting CO_2-to-formate conversion

Received: 6 June 2025

Accepted: 12 January 2026

Published online: 20 January 2026

Check for updates

Yingli Shi[1,3], Ying Liu[2,3], Hongchun Dong[1], Gaocheng Fu[1], Hang Zhou[1], Haifeng Wang[2] ✉, Xue-Lu Wang[1] ✉ & Ye-Feng Yao[1] ✉

The proton-coupled electron transfer (PCET) kinetics plays a critical role in governing the CO_2-to-formate conversion efficiency during CO_2 eletroreduction reaction. While alkali metal cations are known to influence the reaction pathway, elucidating how trace doping modifies the catalytic sites remains a key challenge. Here we show that incorporating Li into bismuth oxycarbonate (BOC-Li) induces structural modifications that optimize the PCET process at bismuth-active sites, thereby boosting CO_2-to-formate conversion. By employing dual-isotope ($^2H/^{13}C$) operando nuclear magnetic resonance (NMR) to track the formation of $^1H^{13}COO^-/^2H^{13}COO^-$, combined with kinetic isotope effect, Tafel analysis and in situ attenuated total reflection surface-enhanced infrared absorption spectroscopy, we observe a more efficient proton-electron transfer pathway. Density functional theory (DFT) calculations suggest that Li doping is associated with enhanced activity of Bi sites, potentially strengthening H_2O/CO_2 adsorption and reducing the O–H activation energy. Collectively, this work highlights alkali doping as a promising strategy for structurally engineering catalytic sites to improve PCET kinetics.

The carbon dioxide reduction reaction (CO_2RR) to value-added chemicals and fuels, particularly when powered by renewable energy sources, offers a sustainable pathway to mitigate fossil fuel dependence and address escalating greenhouse effects[1–3]. However, the CO_2RR process involves intricate multi-step proton-electron transfers steps[4–6]. The proton-coupled electron transfer (PCET) mechanism is pivotal in the electrochemical CO_2RR[7], which relies critically on the dynamic balance among proton supply pathways, electron transfer synergy and intermediate stabilization. Recent optimization strategies for PCET have evolved from singular catalyst design to synergistic regulation of electronic structures and microenvironment engineering. However, challenges persist in dynamically resolving proton sources and transfer pathways, as well as precisely controlling intermediate stability in complex reaction networks. Early theoretical studies revealed the pH- and potential-dependent nature of PCET pathways. For instance, Göttle et al.[8] presented that the CO_2RR pathway of cobalt porphyrin (CoP) catalysts shifts with pH. Specifically, acidic conditions (pH-3.5) favor a sequential proton-electron transfer (SPET) mechanism forming sequential intermediates, while alkaline conditions (pH≥8.3) promote a concerted proton-electron transfer (CPET) process that directly stabilizes key intermediates without discrete protonation steps. Dunwell et al.[9] propose that optimizing experimental conditions, such as employing low overpotentials and minimizing cation-related mass transport limitations, can promote PCET pathways during CO_2RR. Within the kinetically controlled regime, PCET acting as the rate-limiting step enhances the efficiency of coupled proton-electron transfer processes and improves CO selectivity. These studies, however, did not explicitly address the influence

[1]Physics Department & Shanghai Key Laboratory of Magnetic Resonance, School of Physics, Institute of Magnetic Resonance and Molecular Imaging in Medicine, East China Normal University, Shanghai, PR China. [2]State Key Laboratory of Green Chemical Engineering and Industrial Catalysis, Centre for Computational Chemistry and Research Institute of Industrial Catalysis, East China University of Science and Technology, Shanghai, PR China. [3]These authors contributed equally: Yingli Shi, Ying Liu. ✉e-mail: hfwang@ecust.edu.cn; xlwang@phy.ecnu.edu.cn; yfyao@phy.ecnu.edu.cn

of proton sources on pathway selection. Subsequent research by Li et al.[10] achieved 98.1% CO selectivity and presented HCO_3^--involved PCET as the RDS for CO_2RR to CO in aqueous $KHCO_3$ electrolytes, and Zhang et al.[11] lowered the PCET barrier of *OCHO intermediates via Ce-doped Bi by tuning p-band electronic structures. Despite these advances, most studies relied on macroscopic electrochemical data, lacking in-situ tracking of proton transfer dynamics.

To address these limitations, recent efforts have integrated advanced characterization techniques to resolve PCET dynamics. For example, Mukhopadhyay et al.[12] employed operando attenuated total reflection infrared reflection-absorption spectroscopy (ATR-IRRAS) to directly observe the characteristic vibration peak of the *OCHO intermediate (1380 cm^{-1}) within a MOF reservoir (UiO-66-CN) and confirmed through DFT calculations that nitrile groups stabilize intermediates via secondary coordination effects, although proton transport efficiency remained constrained by spatial hindrance in MOF pores. Wang et al.[13] applied in situ attenuated total reflection-surface enhanced infrared absorption spectroscopy (ATR-SEIRAS) to track the sequential PCET pathway in cobalt phthalocyanine-based COFs, revealing that the polarizing effect of hydrated K^+ ions ($[K(H_2O)_n]^+$) weakens the O–H bonds of coordinated water. However, proton sources still predominantly originated from bulk electrolytes. These advancements underscore the critical need to clarify proton origins (e.g., adsorbed water, electrolyte ions, or catalyst active sites) and their transfer pathways.

Alkali metal cations, widely recognized for their promotional effects in CO_2RR, have been studied as electrolyte additives[14,15]. However, recent advancements have shifted focus toward integrating these alkali cations directly into catalyst architectures for performance optimization. For instance, Ding et al.[16] engineered K^+-doped Cu_2Se ($K_{11.2\%}$-Cu_2Se), where embedded K^+ ions stabilized Cu^+ sites, significantly enhancing ethanol selectivity by promoting *CO dimerization. Similarly, Peng et al.[17] demonstrated that S and Na co-doping on bismuth (Bi(110)-S-Na) synergistically localized electrons at *OCHO intermediates while accelerating H^+ generation from water activation, thereby boosting formate production. These studies establish alkali cation-incorporated catalysts as an effective strategy to address the selectivity and activity bottlenecks in CO_2RR systems, thereby offering an effective approach for PCET research.

In this work, we introduce isotope-labeled operando nuclear magnetic resonance (NMR) coupled with a trace Li-incorporated bismuth oxycarbonate (BOC-Li) electrocatalyst to mechanistically probe PCET dynamics in CO_2RR. By employing a dual-tracer approach, using ^{13}C-labeled $^{13}CO_2$ and ^2H-based electrolyte ($K^1H^{12}CO_3/^2H_2O$), our operando ^{13}C NMR protocol reveals distinct $^1H^{13}COO^-$ and $^2H^{13}COO^-$ signals, enabling direct discrimination between HCO_3^-- and solvent-derived proton pathways. Through Li modification the selectivity of formate has been increased from 13.69% to 95.52% at 300 mA cm^{-2}. Besides, the FE_{HCOO^-} reached ~90% even at 1.5 A cm^{-2}. Comparative isotopic analysis between BOC-Li and undoped BOC reveals marked differences in proton transfer mechanisms, elucidating how alkali metal integration influences interfacial PCET kinetics through its effect on the electronic properties of Bi sites. DFT calculations suggest that Li doping on the $Bi_2O_2CO_3$ (161) surface may enhance CO_2RR toward HCOOH by potentially stabilizing four-coordinated Bi sites and promoting the formation of oxygen vacancies (O_v), which could strengthen the adsorption of CO_2 and H_2O. The Li_{3c}-O_v configuration shows relatively favorable catalytic activity in simulations, with a predicted H_2O dissociation barrier of 0.24 eV and a theoretically favorable pathway for HCOOH formation via the *HCOO intermediate. These results indicate possible synergistic effects in reactant adsorption, proton transfer kinetics, and reaction energetics.

Results

Synthesis and characterization of BOC-Li catalyst

Herein, we drew inspiration from Li's unique hydration characteristics among alkali metals[14] to integrate lithium species into the catalyst architecture leading to the creation of the BOC-Li electrocatalyst. The synthesis employed an optimized microwave-assisted protocol[18] followed by sequential LiOH and CO_2 treatments in a controlled sealed environment (see "Methods" section for details). Inductively coupled plasma mass spectrometry (ICP-MS) shows 0.0065 wt% of Li loading (Supplementary Table 1). For comparison, the Li-free BOC was used as the control catalyst.

As depicted in Fig. 1a, the X-ray diffraction (XRD) patterns of both BOC-Li and BOC samples are well-indexed to the orthorhombic phase of $Bi_2O_2CO_3$ (BOC) with the Pna21(33) space group. The (161) plane is identified as the predominant facet. Unlike BOC, the XRD pattern of BOC-Li exhibits noticeable peak broadening, suggesting reduced crystallinity[19]. Furthermore, the enlarged XRD patterns presented in Supplementary Fig. 1 demonstrate a minor angular shift of the BOC-Li diffraction pattern toward higher angle. It may attribute to the doping of Li due to its smaller atomic radius than Bi[20]. The scanning electron microscopy (SEM, Supplementary Fig. 2a) and transmission electron microscopy (TEM, Supplementary Fig. 2b) images show a nanosheet morphology of BOC-Li. Energy-dispersive X-ray (EDX) spectra (Supplementary Fig. 3) confirm the uniform distribution of Bi, O, and C elements throughout the material[21,22]. The high-resolution TEM (HRTEM) image (Fig. 1b) of BOC-Li displays lattice fringes with spacings of 0.295 nm, corresponding to the (161) lattice plane of orthorhombic $Bi_2O_2CO_3$, respectively. In addition, the HRTEM image of BOC-Li reveals a significant presence of lattice distortions and dislocations, which can be attributed to the incorporation of Li[23–26]. For comparison, the HRTEM image of BOC (Fig. 1c) shows well-defined lattice fringes with a spacing of 0.295 nm, corresponding to the (161) lattice plane of BOC. X-ray photoelectron spectroscopy (XPS) was employed to examine the electronic structures of BOC-Li and BOC. The Bi 4*f* XPS spectra (Fig. 1d) for both BOC-Li and BOC exhibit two distinct peaks. The peaks centered at higher binding energies, ~164.49 and 164.2 eV, are attributed to the $4f_{5/2}$ orbital of Bi^{3+}. The peaks at 159.19 and 158.9 eV correspond to the $4f_{7/2}$ orbital of Bi^{3+}[18]. The peaks of BOC-Li shift 0.29 eV towards higher binding energies, indicating a slightly higher oxidation state[27]. The C 1*s* XPS spectrum (Fig. 1e) reveals C–C and C–O peaks at 284.8 and 286.4 eV respectively and that the C=O peak of BOC-Li at 288.9 eV is 0.4 eV higher than that of BOC[7,28].

To resolve the atomic-scale local environment of the incorporated Li species, we employed solid-state ^7Li magic-angle spinning NMR (MAS NMR) spectroscopy. As shown in Fig. 1f, Supplementary Fig. 4 and Supplementary Note 1, the deconvoluted spectrum exhibits two resolved resonances at $\delta = -0.16$ ppm (Site I) and $\delta = -0.53$ ppm (Site II), separated by a chemical shift difference ($\Delta\delta$) of 0.37 ppm (85.30 Hz), confirming the existence of distinct Li coordination geometries. Quantitative integration of these signals yields a population ratio of 40.2% (Site I) to 59.8% (Site II), corresponding to a ratio of 2:3, which is consistent with the predicted dual Li-coordination environments in the crystalline framework. To further elucidate the local coordination of Li dopants, we performed variable-speed ^7Li MAS NMR spectroscopy. As shown in Fig. 1g and Supplementary Note 2, increasing the MAS rate from 8 to 20 kHz results in line narrowing and the emergence of a dominant peak with a discernible shoulder. This spectral evolution confirms that the Li dopants are structurally immobilized within well-defined, yet slightly distinct, lattice sites. The absence of high Li mobility and the discrete nature of these sites strongly support our assignment of Li incorporation into the crystal lattice.

https://doi.org/10.1038/s41467-026-68604-z

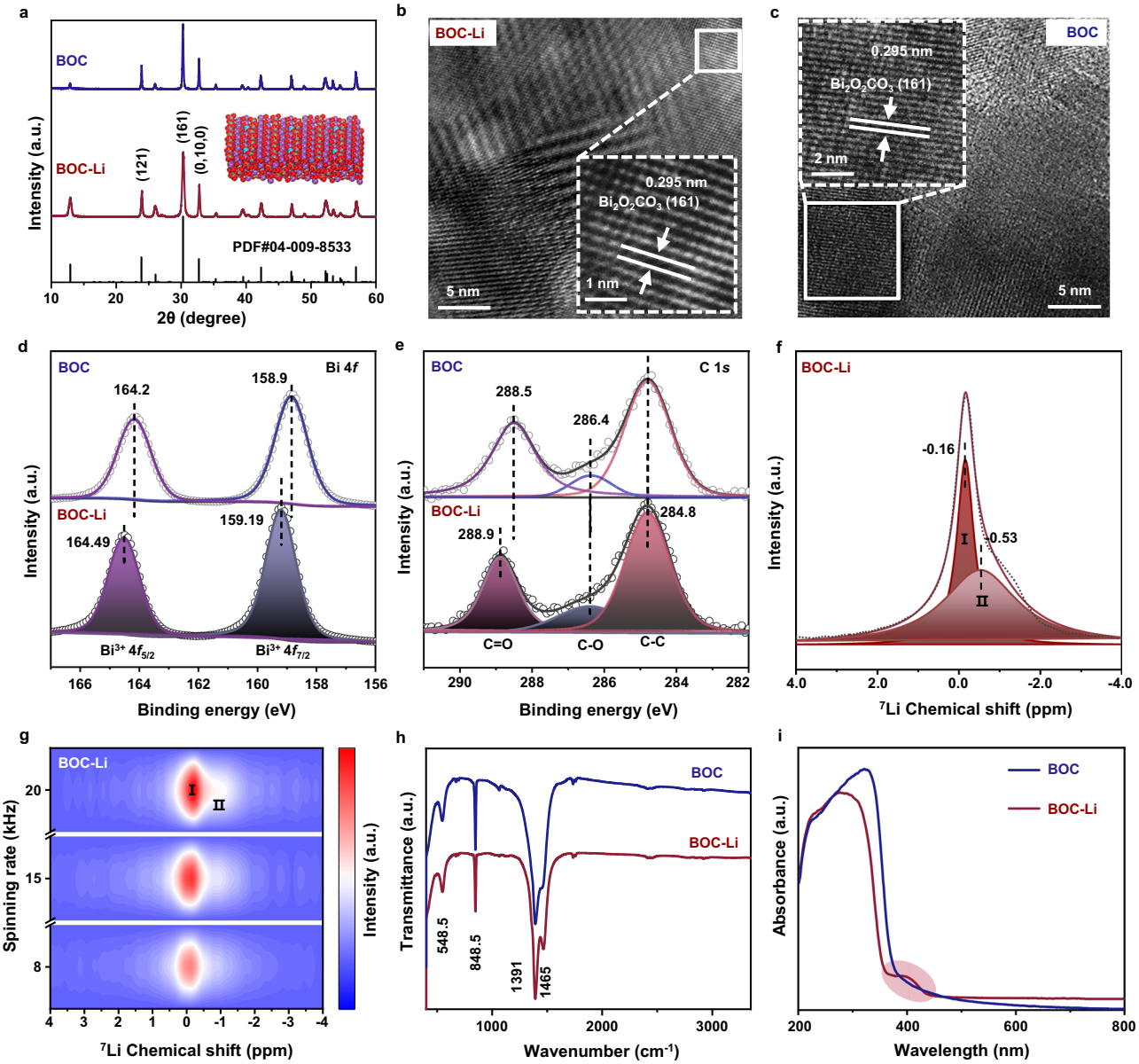

Fig. 1 | Structure characterization of BOC-Li and BOC. a XRD patterns of BOC-Li and BOC indexed to orthorhombic $Bi_2O_2CO_3$. **b** HRTEM image of BOC-Li revealing lattice distortions and dislocations. **c** HRTEM image of BOC with well-defined lattice fringes. **d** Bi 4*f* XPS spectra indicating a higher oxidation state in BOC-Li. **e** C 1*s* XPS spectra showing a higher binding energy for the C=O peak in BOC-Li. **f** Deconvoluted ^{7}Li MAS NMR spectrum showing two Li environments. **g** Variable-speed ^{7}Li MAS NMR of BOC-Li showing signal narrowing and a resolved shoulder, characteristic of Li incorporation into discrete lattice sites. **h** FTIR spectra displaying enhanced absorption at 1465 cm^{-1} in BOC-Li, suggesting altered carbonate bonding. **i** UV-vis absorption spectra of BOC-Li and BOC. Source data are provided as a Source Data file.

Furthermore, the Fourier transform infrared (FTIR) spectrum of BOC-Li (Fig. 1h) resembles that of BOC, exhibiting key vibrational modes including Bi-O stretching vibrations at 548.5 cm^{-1}, out-of-plane bending modes of υ_2 CO_3^{2-} at 848.5 cm^{-1}, and C−O stretching vibrations of (CO_3^{2-}) at 1391 and 1465 cm^{-1}. A notable difference is observed at the 1465 cm^{-1} peak, where BOC-Li displays a more pronounced absorption compared to BOC[29]. Comparative analysis of UV–Vis absorption spectra reveals a difference between BOC and BOC-Li systems (Fig. 1i). While pristine BOC shows no absorption in this region, BOC-Li displays a pronounced spectral feature centered at ~400 nm, likely corresponding to the emergence of a Li-associated coordination complex species.

CO_2RR performance evaluation and mechanism investigation

The CO_2RR performance was initially evaluated in a standard three-electrode H cell using CO_2-saturated 0.5 M $KHCO_3$ electrolyte. The gaseous and liquid products were quantified by gas chromatography (GC) and NMR spectroscopy, respectively[6,30]. As shown in Fig. 2a and Supplementary Fig. 5, BOC-Li exhibits higher selectivity toward formate than the pristine BOC catalyst, achieving high faradaic efficiency (FE) across a wide potential window while effectively suppressing the formation of CO and H_2. Linear sweep voltammetry (LSV) measurements (Supplementary Fig. 6) indicate that BOC-Li attains a higher current density (−295 mA cm^{-2} at −2.0 V vs. RHE, RHE calibration in Supplementary Fig. 7, without iR compensation) compared to BOC (−200 mA cm^{-2}). Electrochemical impedance spectroscopy (EIS) was employed to probe the interfacial charge transfer kinetics. The Nyquist plots in Fig. 2b show a discernibly smaller semicircle diameter in the high-frequency region for BOC-Li, indicating a decrease in charge transfer resistance. Together, these results—demonstrating higher selectivity, activity, and charge transfer efficiency—collectively verify the better CO_2-to-formate conversion capability of BOC-Li in the H-cell setup.

https://doi.org/10.1038/s41467-026-68604-z

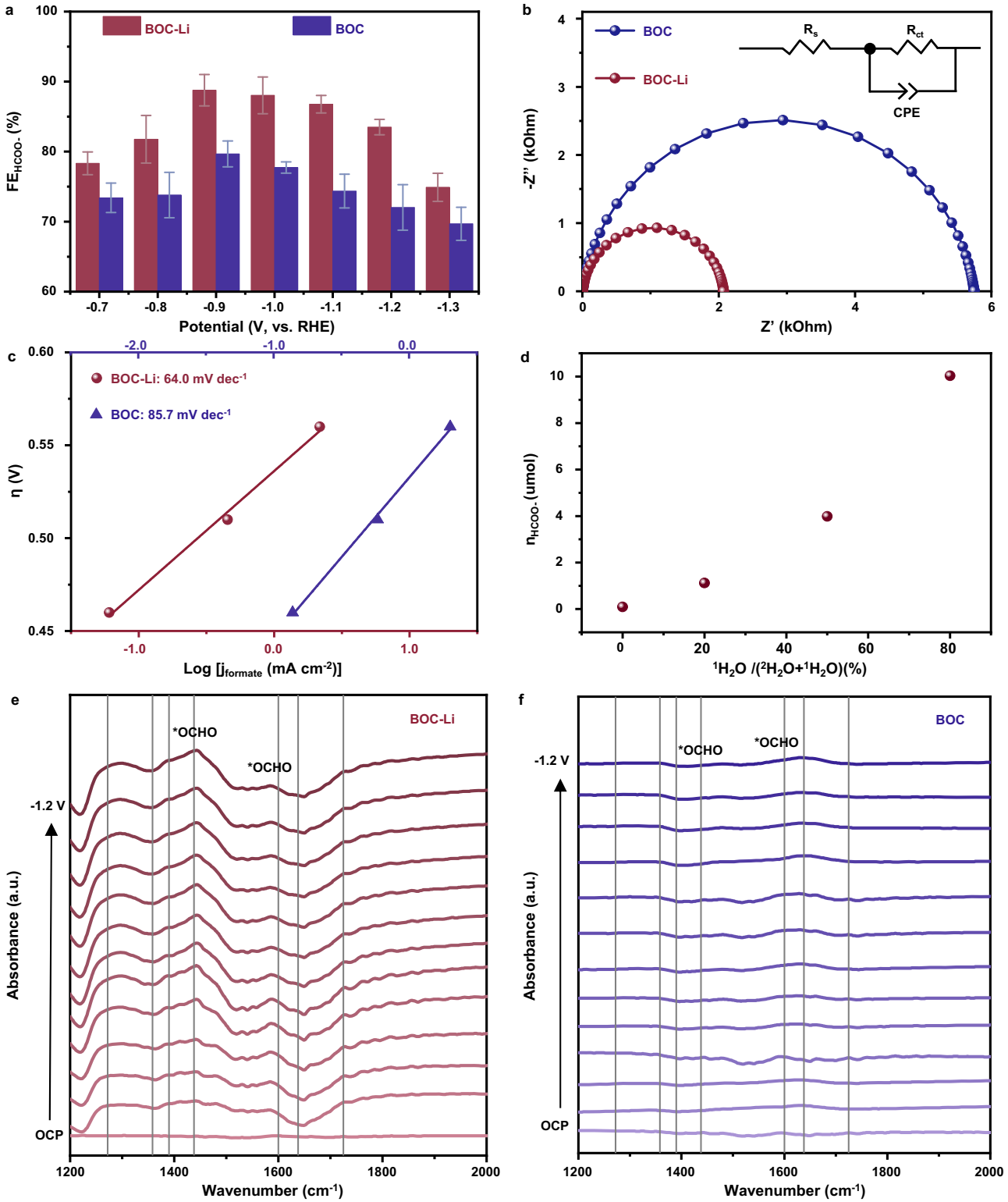

Fig. 2 | Enhanced CO_2RR performance, mechanism and kinetics of BOC-Li. **a** Potential-dependent FE of formate using an H cell in CO_2-saturated 0.5 M $KHCO_3$ (pH = 7.27 ± 0.04, n = 3) for BOC-Li and BOC with mass loading as 1 mg cm^{-2}. The CO_2 flow rate was 20 sccm at room temperature. All potentials reported are non-iR corrected. The error bars represent standard deviations from three independent measurements. **b** Nyquist plots demonstrating the reduced charge transfer resistance of BOC-Li (R_s = 3.8 ± 0.2 Ω, n = 3) relative to BOC (R_s = 3.4 ± 0.3 Ω, n = 3) at −0.27 V in H-cell. All potentials reported are non-iR corrected. **c** The 64.0 mV/dec^{-1} Tafel slope on Li-doped catalyst versus 85.7 mV/dec^{-1} on BOC indicates a concerted proton-electron transfer pathway. **d** Formate yield decreases with higher ^2H_2O content, showing a deuterium KIE that identifies proton transfer as rate-determining. **e**, **f** In situ ATR-SEIRAS shows potential-dependent *OCHO intermediate (1438, 1600 cm^{-1}) only on BOC-Li, validating its facilitated proton-coupled electron transfer. The mass loading was 2 mg cm^{-2}. Source data are provided as a Source Data file.

To probe the origin of the enhanced catalytic performance, we investigated the reaction kinetics. The Tafel slope for formate production on BOC-Li is 64.0 mV dec^{-1}, substantially lower than the 85.7 mV dec^{-1} value measured for undoped BOC (Fig. 2c). A Tafel slope near 60 mV dec^{-1} is consistent with a concerted proton-electron transfer (CPET) process. This interpretation is further supported by a deuterium kinetic isotope effect (KIE), wherein the formate production yield decreases monotonically as the ^2H_2O content in the electrolyte increases (Fig. 2d), confirming that proton transfer is involved in the rate-determining step[6]. Furthermore, this enhanced kinetics is facilitated by an improved reactant affinity, as solution-phase ^{13}C NMR measurements revealed a stronger CO_2 adsorption capacity for BOC-Li compared to BOC (Supplementary Fig. 8 and Supplementary Note 3).

To gain further mechanistic insight into the PCET process, we performed in situ ATR-SEIRAS. The spectra show characteristic peaks at 1438 and 1600 cm^{-1}, which are assigned to the adsorbed *OCHO intermediate[31–37]. Additional spectral features are identified as follows: peaks at ~1272 cm^{-1} correspond to $*CO_2^-$ [37,38], the bands at ~1358 and ~1390 cm^{-1} are attributed to bicarbonate (HCO_3^-) and carbonate (CO_3^{2-}), respectively[39–42], and the peak at ~1638 cm^{-1} is assigned to the O–H bending mode of water[33,40,43–45], based on our control experiments (Supplementary Figs. 9 and 10) and literature references. On BOC-Li, the *OCHO-related peaks at 1438 and 1600 cm^{-1} emerge and intensify at more negative potentials (Fig. 2e), whereas these features remain weak on undoped BOC (Fig. 2f). The potential-dependent formation and stabilization of this key intermediate indicate that the local environment of BOC-Li is favorable for the PCET step. Together, these spectroscopic data provide direct evidence that Li^+ doping appears to promote formate production by facilitating a concerted PCET mechanism at the Bi sites.

Unraveling reaction mechanisms with operando NMR

The electrochemical reduction of CO_2 to formate is known to proceed through competing pathways. However, their mechanistic details—particularly concerning protonation sources and oxygen transfer dynamics—remain contentious. Early studies have proposed two possible routes, namely the *OCHO and the *COOH pathways. The former proceeds through an oxygen-bound intermediates with sequential PCET, while the latter requires direct formation of a carbon-bound intermediate[46,47]. To contribute to this discussion, we employed a multimodal operando NMR approach integrating ^1H, ^{17}O, and $^{13}C/^2H$ isotopic tracking, focusing on a comparison between BOC-Li and undoped BOC. Our goal is to examine how Li-induced modifications to the electronic structure of Bi sites influence water-mediated oxygen transfer and protonation dynamics. This is achieved by correlating real-time intermediate speciation with interfacial kinetics under operational CO_2RR conditions.

Operando $^1H/^{17}O$ NMR reveals H_2O-oxygen activation on BOC-Li

Catalytic performance was evaluated in a custom three-electrode NMR microreactor (Supplementary Fig. 11) under continuous CO_2 flow (1.5 standard cubic centimeters per minute, 1.5 sccm) at 298 K, using an isotopically enriched electrolyte (450 µL $^2H_2{}^{16}O$, 50 µL $^1H_2{}^{17}O$ and 25.16 mg $K^1HC^{16}O_3$)[47]. The working electrode was prepared by loading the catalyst onto carbon microfibers, with Pt wire as the counter/reference electrode.

We leveraged synchronized operando $^1H/^{17}O$ NMR to track water-derived oxygen. This enabled the simultaneous quantification of formate (^1H NMR) and oxygenated species (^{17}O NMR), thereby linking product formation to oxygen transfer events. As shown in Fig. 3a, in situ ^1H NMR quantification during 3 h electrolysis at −1.18 V revealed that BOC-Li produced 21 times more formate than the undoped BOC. The formate peak also exhibited a downfield chemical shift of 3.50 Hz (from 8.467 ppm for BOC to 8.472 ppm for BOC-Li). The corresponding ^{17}O NMR spectrum of BOC-Li (Fig. 3b) revealed distinct signals from key oxygenated species. Compared to undoped BOC, these signals exhibited significant downfield shifts: hydrated CO_2 (79.381 ppm, +2.37 Hz), bicarbonate (173.21 ppm, +10.44 Hz), and ^{17}O-formate (288.737 ppm, +25.14 Hz). Moreover, the signal intensity for ^{17}O-formate was greater in BOC-Li.

To track oxygen involvement, we analyzed the ^{17}O distribution in the hydrated CO_2 and formate. The absence of detectable C-^{17}OH signals in formate suggests rapid hydroxyl exchange between reaction intermediates and the solvent water. The transient nature of hydroxyl-bound ^{17}O atoms explains their lack of detection by NMR. Consequently, the ^{17}O NMR resonance at 288.737 ppm is collectively assigned to all ^{17}O-enriched isotopologues ($^1HC^{17}O^{16}O^-$, $^1HC^{17}O^{17}O^-$), serving as a unified spectroscopic marker.

The relationship between oxygen transfer dynamics and catalytic stability was investigated through a multimodal operando NMR approach. By performing synchronized $^1H/^{17}O$ spectroscopy with time-resolved spectral acquisition (30-min intervals over 180 min), we tracked oxygen incorporation pathways. As shown in Fig. 3c and Supplementary Fig. 12, BOC-Li exhibits rapid $HCOO^-$ signal emergence ($\tau_{onset} < 30$ min) with linear concentration growth, indicative of stable redox-active sites and efficient C–H bond formation. In contrast, formate signals for BOC were near the background level and accumulated slowly, indicating its lower activity.

Complementary operando ^{17}O NMR analysis (Fig. 3d and Supplementary Fig. 13) provides insight into the oxygen transfer efficiency underlying these performance differences. For BOC-Li (left panel), distinct ^{17}O-formate resonances (288.737 ppm) appear within 30 min and intensify linearly over 3 h, consistent with rapid oxygen activation and sustained interfacial stability. In contrast, BOC (right panel) shows negligible ^{17}O-formate signals with minimal growth, indicating sluggish oxygen incorporation. This direct temporal correlation between persistent ^{17}O-formate accumulation in BOC-Li and the stagnant signal in BOC aligns with the 21-fold productivity difference (Fig. 3a), strongly ascribing the enhancement to Li doping.

To probe oxygen incorporation pathways during CO_2 electroreduction, we quantified the C=^{17}O isotopologues in the formate products using a published method[47]. The quantitative analysis indicated that ^{17}O-labeled formate constituted 2.46 mol% of the total produced by BOC-Li after 3 h of operation. This value is notably below the theoretical maximum for direct CO_2 -derived oxygen, supporting the dominance of the *OCHO pathway over the *COOH route[47]. In contrast, undoped BOC yielded only 1.50%. This enhanced isotopic incorporation in BOC-Li, resolved by operando $^1H/^{17}O$ NMR, confirms that Li doping promotes water-derived oxygen participation by modifying interfacial oxygen transfer dynamics.

Operando ^{13}C NMR reveals the proton source of $HCOO^-$

To probe proton sourcing, we employed a dual-isotope ($^{13}C/^2H$) operando NMR approach. This method distinguishes protonation pathways by utilizing ^2H-^{13}C J-coupling in the $^2H^{13}COO^-$ product, which discriminates between deuterium from water and protons from bicarbonate under $^{13}CO_2$RR conditions. The operando ^{13}C NMR experiments were conducted in a three-electrode setup with a BOC-Li-modified carbon fiber working electrode, Pt counter/reference electrodes, and a deuterated electrolyte (500 µL ^2H_2O, 25.16 mg $K^1H^{12}CO_3$). Prior to electrolysis, the electrolyte was pre-saturated with $^{13}CO_2$, which was then continuously supplied at 1.5 sccm during electrolysis at −1.28 V to maintain a constant concentration at the gas-liquid interface at 298 K.

As shown in Supplementary Fig. 14, ^1H-decoupled ^{13}C NMR spectroscopy clearly showed signals for solvated $^{13}CO_2$ ($\delta = 124.62$ ppm), bicarbonate ($H^{13}CO_3^-$, $\delta = 160.23$ ppm), and the dominant formate derivatives ($\delta = 170$-172 ppm). High-resolution spectral deconvolution in ^2H_2O (Fig. 3e, blue bottom trace and Supplementary Note 4) revealed two distinct formate configurations. A diagnostic 1:1:1 triplet

https://doi.org/10.1038/s41467-026-68604-z

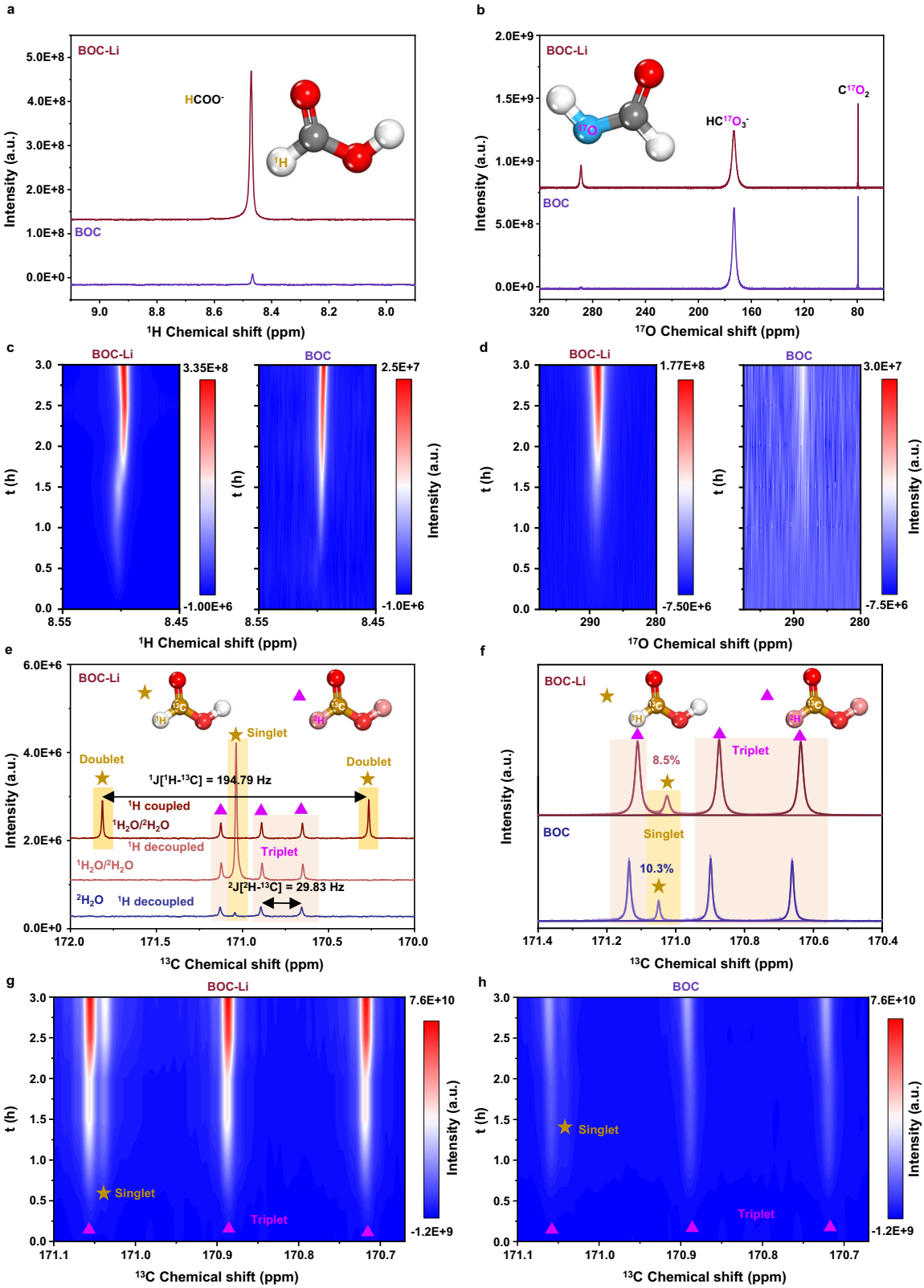

(δ = 170.89 ppm, purple triangles, $^{2}J[^{2}H\text{-}^{13}C]$ = 29.83 Hz) was assigned to $^{2}H^{13}COO^{-}$, arising from scalar coupling between ^{13}C and the bonded deuterium (n = 1, ^{2}H, I = 1). Concurrently, a singlet at δ = 171.04 ppm (golden star) corresponds to $^{1}H^{13}COO^{-}$. The triplet serves as a spectroscopic fingerprint for α-carbon-selective deuteration, while the singlet indicates the coexistence of protonated isotopologues. This dual-isotope strategy effectively distinguishes protonation pathways: deuterium from interfacial water ($^{2}H^{13}COO^{-}$) versus protons from bicarbonate ($^{1}H^{13}COO^{-}$), providing strong evidence for deuteration dynamics and proton transfer selectivity.

The key finding is that formate formation is dominated by protons derived from water, as unambiguously resolved by their distinct J-coupling signatures. To gain further insight into interfacial proton transfer dynamics, we performed controlled ^{13}C NMR in a mixed

Fig. 3 | Operando NMR mechanistic investigation of CO_2RR on BOC-Li versus BOC catalysts. a Time-resolved ^{1}H NMR analysis quantifies 21-fold enhanced formate production on BOC-Li. **b** ^{17}O NMR spectra distinguish oxygen speciation (hydrated CO_2,79.38 ppm; HCO_3^-, 173.21 ppm; formate, 288.74 ppm). **c** Operando ^{1}H NMR profiles reveal BOC-Li's rapid formate generation versus BOC's negligible activity. **d** Operando ^{17}O NMR spectra demonstrate progressive ^{17}O-formate accumulation on BOC-Li, contrasting with BOC's background-level signals. **e** Key Information Summary: Dual-isotope (^{2}H/^{13}C) NMR spectroscopy in a mixed $^1H_2O/^2H_2O$ electrolyte directly identifies and distinguishes both protonated ($^1H^{13}COO^-$) and deuterated ($^2H^{13}COO^-$) formate species through their characteristic J-coupling patterns. This provides direct evidence that protons derived from water dissociation dominate the formate formation pathway during CO_2 reduction. Detailed description: $^2H^{13}COO^-$ is identified by its characteristic 1:1:1 triplet (purple triangles, $^2J[^2H\text{-}^{13}C]$ = 29.83 Hz, pink shading). $^1H^{13}COO^-$ is identified as a singlet upon ^{1}H-decoupling (golden star, pink trace, light yellow shading) and as a 1:1 doublet under ^{1}H-coupled conditions (golden stars, red trace, $^1J[^1H\text{-}^{13}C]$ = 194.79 Hz, yellow shading). **f** ^{13}C NMR results quantify reduced ^{1}H/^{2}H ratios (8.5% vs 10.3%) in BOC-Li, indicating preferential interfacial hydration over bicarbonate pathways. Operando ^{13}C NMR tracks the proton source for formate generation. Spectra for **g** BOC-Li and **h** BOC show the accumulating of both protonated ($^1H^{13}COO^-$, golden star) and deuterated ($^2H^{13}COO^-$, purple triangles) formate species. (a-d) CO_2 flow rate: 1.5 sccm; electrolyte: 450 µL $^2H_2{}^{16}O$ + 50 µL $^1H_2{}^{17}O$ + 25.16 mg $K^1H^{16}O_3$. **e**–**h** $^{13}CO_2$ flow rate: 1.5 sccm; electrolyte: 500 µL ^2H_2O + 25.16 mg $K^1H^{12}CO_3$. The prominent formation of deuterated formate in BOC-Li implicates water (^2H_2O) as the primary proton donor. Source data are provided as a Source Data file.

$^2H_2O/^1H_2O$ electrolyte (1:1 v/v, 25.16 mg $K^1H^{12}CO_3$, $^{13}CO_2$-saturated; Fig. 3e and Supplementary Note 4). Firstly, the diagnostic $^2H^{13}COO^-$ triplet (δ = 170.89 ppm, purple triangles, 1:1:1, $^2J[^2H\text{-}^{13}C]$ = 29.83 Hz) remained well-resolved, confirming persistent ^{2}H-^{13}C coupling. Secondly, in the decoupled spectra (pink middle trace), the $^1H^{13}COO^-$ singlet (δ = 171.04 ppm, golden star) intensified relative to pure ^2H_2O conditions, consistent with greater proton availability from enhanced ^1H_2O auto-protolysis and $K^1H^{12}CO_3$ dissociation in the mixed phase. Finally, in the coupled spectrum (red top trace), the $^1H^{13}COO^-$ signature appeared as a 1:1 doublet (δ = 171.04 ppm, golden stars, $^1J[^1H\text{-}^{13}C]$ = 194.79 Hz), demonstrating the distinct NMR signature of spin-$^1/_2$ protons (doublet). The simultaneous detection of deuterated (triplet) and protonated (doublet/singlet) adducts showcases the power of this dual-isotope operando NMR approach for tracking proton transfer pathways and interfacial deuteration kinetics.

The catalytic selectivity and proton transfer dynamics of CO_2RR were probed using a multimodal NMR approach integrating ^{1}H, ^{13}C, and ^{2}H isotopic tracing. For BOC-Li, operando ^{1}H NMR revealed a characteristic α-proton doublet for $^1H^{13}COO^-$ (δ = 8.465 ppm, $^1J[^1H\text{-}^{13}C]$ = 194.79 Hz; Supplementary Fig. 15), confirming high isotopic fidelity. Complementary ^{13}C NMR (Supplementary Fig. 16) and ^{2}H NMR (Supplementary Fig. 17) spectra differentiated protonation pathways: the ^{13}C NMR spectrum resolved the $^2H^{13}COO^-$ triplet (from water) and the $^1H^{13}COO^-$ singlet, while the ^{2}H NMR spectrum showed the corresponding $^2H^{13}COO^-$ doublet ($^2J[^2H\text{-}^{13}C]$ = 29.83 Hz, from bicarbonate). This pronounced isotopic discrimination, which correlates with BOC-Li's higher performance, indicates that Li doping tunes the electronic structure of Bi active sites, thereby modulating proton transfer kinetics.

This interpretation is further supported by controlled electrolysis in 0.5 M $K^1H^{12}CO_3$ (Fig. 3f). Spectral deconvolution showed that the $^1H^{13}COO^-/^2H^{13}COO^-$ ratio was lower for BOC-Li (8.5%) than for BOC (10.3%), indicating a relative decrease in bicarbonate-mediated protonation and a correspondingly greater reliance on water-derived protons for BOC-Li. This isotopic preference, which aligns with BOC-Li's higher Faradaic efficiency, indicates that Li doping modifies the electronic structure of Bi sites, thereby promoting CO_2 pre-activation and stabilizing the *OCHO intermediate.

The proton transfer pathways and carbon speciation during $^{13}CO_2$RR were tracked by synchronized operando ^{1}H and ^{13}C NMR at −1.28 V over 3 h. Comparative ^{1}H NMR (Supplementary Figs. 18 and 19) showed persistently higher and faster formate production for BOC-Li (signal growth at δ = 8.465 ppm). Complementing this, time-resolved ^{13}C NMR (Fig. 3g, h, and Supplementary Fig. 20) clearly distinguished the $^2H^{13}COO^-$ triplet from the $^1H^{13}COO^-$ singlet, revealing a systematically stronger progression of the water-derived $^2H^{13}COO^-$ signal for BOC-Li. This consistent kinetic advantage is attributed to Li-mediated tuning of the Bi sites, which enhances water-derived proton transfer. Thus, this multimodal approach not only distinguishes catalytic pathways but specifically reveals how Li doping steers the PCET mechanism toward a water-mediated route.

DFT calculation

To elucidate the Li-mediated activity of HCOOH formation, first-principles DFT calculations were systematically performed. As depicted in Fig. 4a, the predominant $Bi_2O_2CO_3$ (161) surface identified through XRD analysis comprises four/three-coordinated Bi (Bi_{4c}/Bi_{3c}) and four/three-coordinated oxygen (O_{4c}/O_{3c}) atoms. Computational simulations suggested two distinct Li-doping sites on this surface, both of which induced spontaneous oxygen vacancy (O_v) formation, as illustrated in the structural models (Supplementary Fig. 21). The computational analysis indicates Li dopants tend to stabilize at four-coordinated sites (Li_{4c}), with a thermodynamic advantage of 0.32 eV over three-coordinated sites (Li_{3c}). It is worth noting that Li doping promotes the formation of surface O_v, which are predicted to act as new reaction centers (Supplementary Fig. 22). Additionally, Bader charge analysis suggests that Li_{4c} exhibits a relatively lower charge state (+0.90 |e|) compared to Li_{3c} (+0.92 |e|). These theoretical insights offer a mechanistic rationalization for the experimentally observed observations of dual Li species populations.

To elucidate the role of Li doping in catalytic activity, we systematically investigated CO_2RR with H_2O as the proton source. On the pristine $Bi_2O_2CO_3$(161) surface, H_2O adsorbs at Bi_{4c} and Bi_{3c} sites with comparable energies of −0.77 eV and −0.79 eV, respectively (Fig. 4b, and Supplementary Fig. 23). In contrast, Li-doped configurations exhibit stronger H_2O adsorption strength at O_v sites, with the adsorption energies of −0.80 eV (Li_{3c}-doped) and −0.91 eV (Li_{4c}-doped) (Fig. 4d). For CO_2, the molecule preferentially binds at the Bi_{3c}-O_{3c}-Bi_{3c} bridge site on the pristine surface, adopting a bent configuration and an adsorption energy of −0.54 eV (Fig. 4c, and Supplementary Table 2). Upon Li doping, CO_2 adsorption is also enhanced, with adsorption energies of −0.75 eV (Li_{4c}-doped) and −0.69 eV (Li_{3c}-doped) compared to the undoped surface (Fig. 4d, and Supplementary Fig. 24), suggesting stronger surface interactions. This progressive increase in adsorption strength appears to correlate with improved CO_2 surface coverage, suggesting that Li incorporation may facilitate CO_2RR by optimizing the thermodynamics of reactant adsorption.

Moreover, H_2O dissociation appears to be facilitated on the Li-doped surface. As shown in Fig. 4e and Supplementary Fig. 25, the energy profiles reveal a marked reduction in the activation energy (E_a) of O–H bond cleavage at O_v sites on the Li-doped surfaces, decreasing to 0.34 eV for Li_{4c}-doped and 0.24 eV for Li_{3c}-doped configurations, compared to 0.40 eV and 0.36 eV at Bi_{4c} and Bi_{3c} sites on the pristine surface. Notably, the Li_{3c}-doped configuration, in particular, exhibits a more thermodynamically favorable H_2O dissociation, with an exothermic energy of −0.43 eV, outperforming other reactive sites. We also compared the H_2O dissociation at non-oxygen-vacancy sites on Li-doped $Bi_2O_2CO_3$(161) surfaces, further confirming the active Li-doped surface compared to clean surface (Supplementary Fig. 26, and Supplementary Note 5). These results suggest that Li incorporation may promote H_2O dissociation, potentially increasing proton availability for subsequent catalytic steps.

https://doi.org/10.1038/s41467-026-68604-z

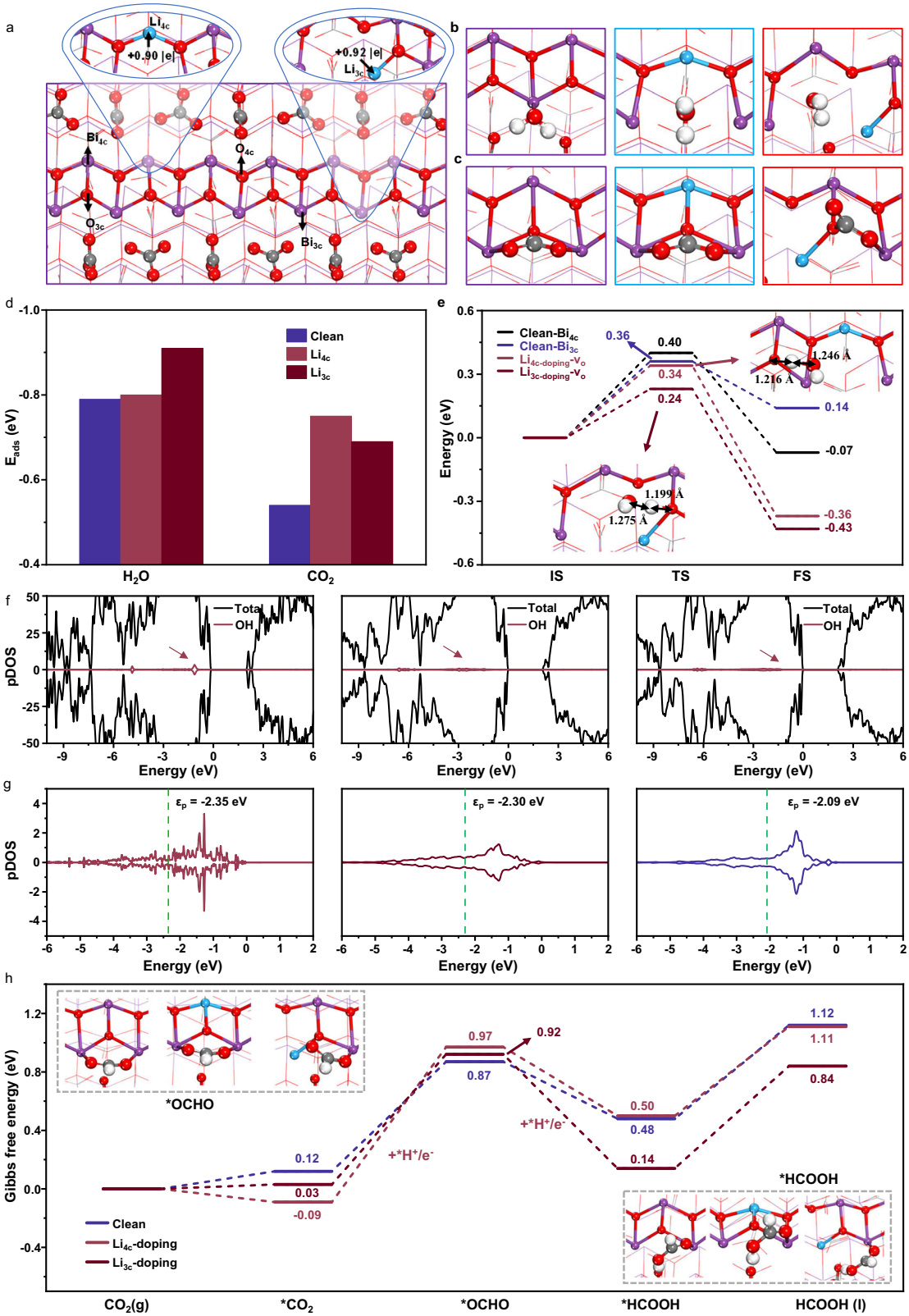

Fig. 4 | Effects of Li doping on surface structure, adsorption, and reaction energetics of $Bi_2O_2CO_3$(161). a The structure of $Bi_2O_2CO_3$(161) surface with Li_{4c} and Li_{3c} doped marked. The best adsorption structure of H_2O (**b**) and CO_2 (**c**) at clean, Li_{4c}- and Li_{3c}- doped surfaces. **d** The adsorption energy of H_2O and CO_2 at clean, Li_{4c}- and Li_{3c}- doped surfaces. **e** The energy profiles of H_2O dissociation at the clean, Li_{4c} and Li_{3c}-doping surface. **f** Projected density of states (PDOS) of OH group on the clean surface and on the Li_{3c}- and Li_{4c}-doped surfaces. **g** PDOS of lattice oxygen atom on the clean surface and on the Li_{3c}- and Li_{4c}-doped surfaces, with the corresponding *p*-band center (ε_p) indicated. **h** Free energy diagrams for HCOOH formation via the *OCHO mechanism. Purple, Bi; red, O; white, H; grey, C; light blue, Li. These color notations are used throughout the paper. Source data are provided as a Source Data file.

https://doi.org/10.1038/s41467-026-68604-z

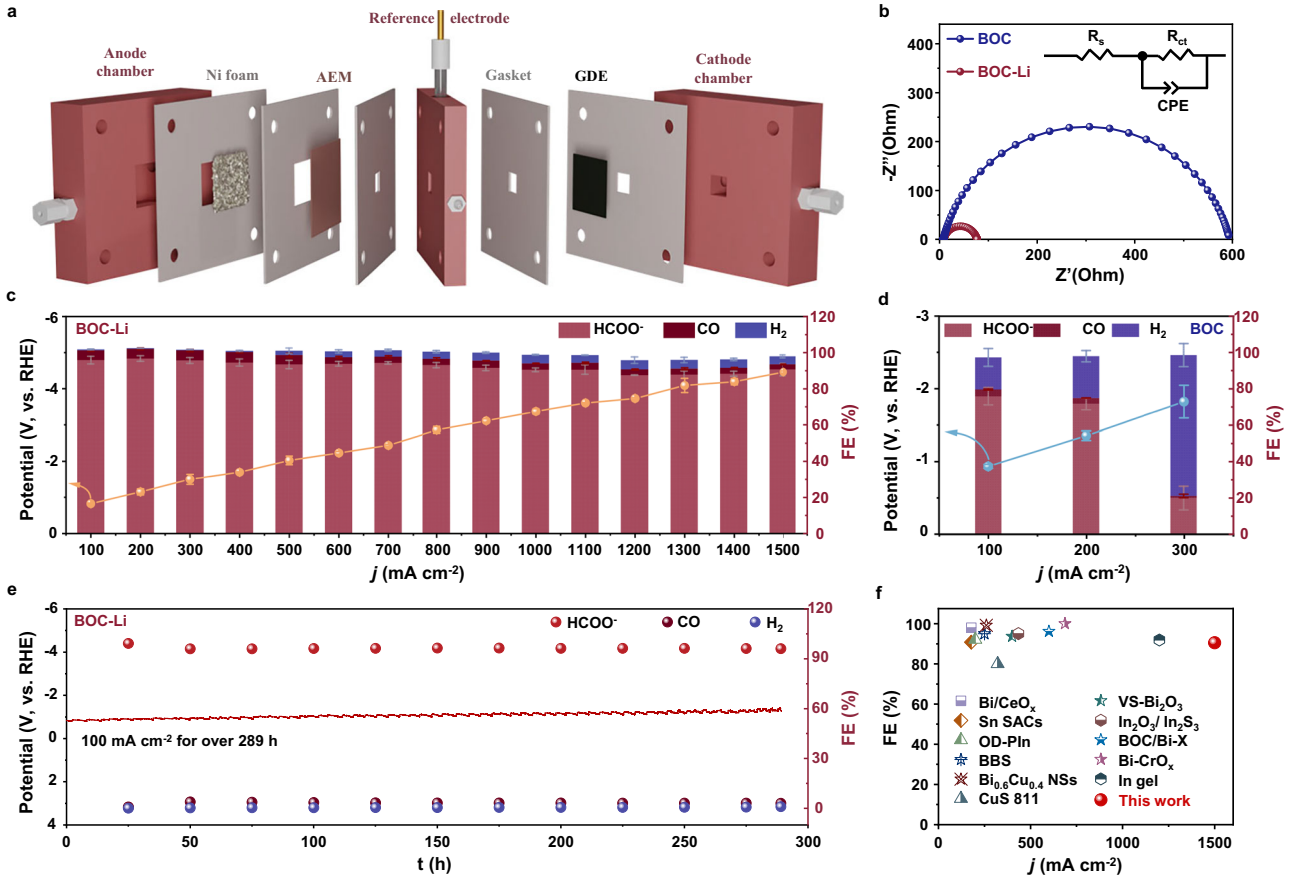

Fig. 5 | CO_2RR performance of BOC-Li and BOC in flow cell. a Three-electrode flow cell for CO_2RR in 1.0 M KOH (pH = 13.98 ± 0.03, n = 3, flow rate: 25 mL min^{-1}) with CO_2 flow at 20 sccm at room temperature. **b** Nyquist plot showing reduced charge transfer resistance for BOC-Li (R_s = 9.0 ± 0.1 Ω, n = 3) compared to BOC (R_s = 7.9 ± 0.3 Ω, n = 3) in flow cell at −0.37 V. **c** CO_2RR performance plot of BOC-Li shows FE_{HCOO^-} ~90% at 100-1500 mA cm^{-2}. **d** CO_2RR performance plot of BOC exhibits lower FE_{HCOO^-}. **e** Stability analysis of BOC-Li remains stable over 289 h at 100 mA cm^{-2} with the FE_{HCOO^-} over 95%. All potentials reported are non-iR corrected. The error bars represent standard deviations from three independent measurements. **f** Formate selectivity and current density of the BOC-Li catalyst compared with recent formate-selective catalysts (Supplementary Table 3). Catalyst loading: 1.25 mg cm^{-2}. Source data are provided as a Source Data file.

To elucidate the origin of the lower activation barrier for water dissociation on the Li_{3c}-doped surface, electronic structure analyzes were performed. The projected density of states (pDOS) analysis shows that for the clean surface, OH^- adsorption induces a narrow peak slightly below the conduction band minimum (CBM), whereas on the doped surface a broader peak appears further below the CBM, indicating stronger orbital hybridization with Bi and enhanced bonding stability (Fig. 4f). In addition, the p-band center of surface O_{latt} on the doped surface, particularly for Li_{3c} doping, is shifted upward relative on the clean surface, which enhances H^+ adsorption and further stabilizes the reaction intermediates (Fig. 4g). These results collectively suggest that Li_{3c} doping modifies the surface electronic structure in a way that stabilizes both OH and H species, thereby facilitating water dissociation. It is also worth noting that the stronger binding of H^+ could suppress the H–H coupling process, making the formation of H_2 less thermodynamically favorable and consequently reducing its selectivity, which is consistent with the experimental observation.

To further evaluate the effect of Li-doping, the CO_2RR to HCOOH was examined on pristine, Li_{4c}-, and Li_{3c}-doped surfaces. Free energy profiles for HCOOH formation via the *OCHO pathway (Fig. 4h, Supplementary Fig. 27, and Supplementary note 6) indicate that the initial hydrogenation step ($*CO_2 + *H^+/e^- \rightarrow *OCHO$) requires a noticeable energy input, followed by an exothermic hydrogenation step leading to HCOOH formation. Comparative analysis suggests that the Li_{3c}-doped surface appears to exhibit the lowest overall energy requirement for HCOOH production among the three configurations, implying a potentially higher catalytic efficiency. These results point to Li_{3c}-doping as a potentially favorable configuration for promoting HCOOH synthesis. More broadly, these findings support Li incorporation as a promising strategy to modulate CO_2RR activity, with site-specific doping suggested as a possible route for tuning catalytic performance.

Flow-cell CO_2RR performance

To assess the commercial potential of BOC-Li for CO_2-to-formate conversion, we evaluated its performance across a range of current densities in a flow cell reactor (Fig. 5a) in 1.0 M KOH electrolyte[48]. LSV shows that BOC-Li delivers a 28% higher current density than BOC (−1762 vs. −1381 mA cm^{-2} at −4.97 V vs. RHE, Supplementary Fig. 28). This is accompanied by a doubled double-layer capacitance (C_{dl}), with measured values of 9.34 vs. 4.39 mF cm^{-2} for BOC-Li and BOC, respectively (Supplementary Fig. 29), indicating a likely increase in the electrochemical active surface area. This is further supported by a lower charge transfer resistance, as evidenced by the smaller semicircle in the Nyquist plot (Fig. 5b).

BOC-Li exhibits better CO_2-to-formate performance across a wide current density range (100-1500 mA cm^{-2}), sustaining a FE of ~90% with marginal decay at industrially relevant current densities (Fig. 5c). Notably, it achieves an FE of 95.5% at 300 mA cm^{-2} and a low potential of −1.50 V, whereas the undoped BOC catalyst only reaches 13.7% at a more negative potential of −2.07 V under the same condition (Fig. 5d).

This performance disparity underscores the critical role of Li doping in enhancing both activity and selectivity. Furthermore, BOC-Li demonstrates robust operational stability over 289 h at 100 mA cm^{-2} with the FE_{HCOO-} over 95% (Fig. 5e), and its overall performance is highly competitive among state-of-the-art formate-selective electrocatalysts (Fig. 5f, and Supplementary Table 3).

Post-reaction characterization confirms the structural stability of the BOC-Li catalyst. SEM imaging shows that the nanosheet morphology is preserved after electrolysis (Supplementary Fig. 30). XRD patterns demonstrate that the crystal structure of orthorhombic $Bi_2O_2CO_3$ remains intact (Supplementary Fig. 31). XPS analysis indicates that the Li-modified oxidation state of Bi is maintained (Supplementary Fig. 32). Furthermore, ex situ ^{7}Li MAS NMR spectra confirm that the two distinct Li sites remain structurally stable (Supplementary Fig. 33). These results collectively illustrate the structural and compositional integrity of BOC-Li under CO_2RR conditions.

Extension to other alkali dopants

To systematically explore the broader potential of our approach, we extended the doping strategy to include Na^+ and K^+. Under identical synthesis conditions, both dopants were successfully incorporated into the BOC structure, as confirmed by comprehensive characterization. Similar to the Li^+-modified catalyst, these alkali-doped variants exhibited universally enhanced electrochemical properties, including increased active surface area and improved charge transfer kinetics compared to pristine BOC (Supplementary Figs. 34–52). This common improvement translated directly to catalytic performance, with BOC-Na and BOC-K achieving high $FE_{formate}$ at low-to-medium current densities. Operando NMR spectroscopy further verified that both dopants promoted the water-derived protonation pathway, confirming that the enhanced PCET mechanism represents a general phenomenon across alkali-modified catalysts.

The investigation reveals that while the fundamental enhancement in PCET kinetics is a general characteristic of alkali doping, the specific choice of dopant determines the operational stability under practically relevant conditions. Although all doped catalysts performed comparably at moderate current densities, BOC-Li demonstrated better performance maintenance, sustaining >90% $FE_{formate}$ across an extended operating range up to 1100 mA cm^{-2}, while the performance of BOC-Na and BOC-K began to decay beyond 500 mA cm^{-2}. This systematic study establishes alkali doping as a promising strategy for modulating PCET kinetics in CO_2-to-formate conversion, with Li^+ emerging as the optimal dopant for applications requiring sustained high-current operation.

Discussion

This study demonstrates that Li doping in bismuth oxycarbonate (BOC-Li) improves CO_2-to-formate conversion, achieving ~90% formate selectivity at 1.5 A cm^{-2} with sustained operational stability (>289 h at 100 mA cm^{-2}). We find that this enhancement is consistent with Li modulating the electronic structure of Bi sites, which appears to optimize the PCET kinetics. Dual-isotope (^{2}H/^{13}C) operando NMR identifies interfacial water as the primary proton donor, supported by a reduced $^1H^{13}COO^-/^2H^{13}COO^-$ ratio (8.5% vs. 10.3%) and intensified $^2H^{13}COO^-$ triplet progression in BOC-Li. This mechanistic shift is corroborated by kinetic analyzes and in situ ATR-SEIRAS, which indicate accelerated water dissociation and stabilization of the *OCHO intermediate. DFT calculations provide further insight, suggesting that Li-doping may strengthen H_2O/CO_2 adsorption and lower the H_2O deprotonation barrier, thereby offering a plausible explanation for the experimentally observed preference toward the water-mediated pathway. Overall, this work highlights alkali doping as a promising strategy for structurally tuning catalytic sites to influence PCET mechanisms.

Looking forward, the multimodal operando NMR methodology established here holds broader utility for deciphering complex reaction networks. Our preliminary ^{13}C NMR analysis of ethanol models (Supplementary Fig. 53 and Supplementary Note 7) suggests that the distinct signatures of ^{1}H- and ^{2}H-labeled groups can be retained in mixed solutions. This observation demonstrates the potential to track proton transfer and carbon origin in multi-carbon products such as ethanol and acetate. Extending this strategy to actual CO_2 electrolysis for C_{2+} products represents a promising future direction for elucidating the intertwined PCET and C–C coupling mechanisms at catalytic interfaces.

Methods

Chemicals

The following chemicals were acquired from their respective suppliers for the project: Bismuth (III) nitrate pentahydrate ($Bi(NO_3)_3{\cdot}5H_2O$, 99.0%) and a 5% Nafion 117 solution (5% in a mixture of lower aliphatic alcohol and water) were sourced from Shanghai Macklin Biochemical Technology Co., Ltd. Dicyandiamide (DCD, 99%) was provided by J&K Scientific Ltd. Shanghai Titan Scientific Co., Ltd was the supplier for Ethylene glycol (EG, 99%), potassium hydroxide (KOH, 90.0%), lithium hydroxide (LiOH, 99%), potassium bicarbonate ($KHCO_3$, 99.5%), and ethanol (EtOH, 99.7%). Deuterium oxide (^2H_2O, 99.9%) was obtained from Qingdao Tenglong Microwave Technology Co., Ltd, and isopropanol (PrOH, 99.7%) was supplied by Shanghai Aladdin Biochemical Technology Co., Ltd. All chemicals were used as received, without further purification. Deionized (DI) water for our experiments was provided by the LICHEN System (UPTA-10).

Synthesis of Bi-based precursor

The Bi-based precursor was synthesized using a refined microwave-assisted ultrasonic method[18]. Initially, 2 mmol of $Bi(NO_3)_3{\cdot}5H_2O$ and 30 mmol of dicyandiamide were dissolved sequentially in 100 mL of ethylene glycol (EG) under ultrasonic agitation to form a clear solution. This was performed in a specialized three-neck flask.

The flask was then connected to a microwave/ultrasonic synthesizer (XH-300A, Beijing Xianghu Science and Technology Development Co., Ltd), equipped with a condensation setup. The reaction was conducted under a constant temperature mode, with microwave and ultrasonic powers both set to 500 W. The temperature was ramped to 150 °C within 10 min and maintained for 20 min using an automated program.

The resulting white precipitate was collected by centrifugation and washed thoroughly with deionized water and ethanol to remove impurities. The final product was obtained as a white powder after drying at 60 °C for 12 h in a vacuum oven.

Synthesis of BOC-Li

The synthesized Bi-based precursor was subjected to further modification using carbon dioxide (CO_2) as both a reactant and a means to create a high-pressure environment, in conjunction with a lithium hydroxide (LiOH) solution. The process involved adding 300 mg of the Bi-based precursor into a 20 mL reaction vessel containing 2 mL of a 0.5 M LiOH solution. The vessel was then sealed and charged with 50 mL of CO_2 gas to facilitate the reaction under high-pressure conditions. After 3 h of ultrasonication to promote complete mixing and reaction, the white precipitate formed was collected by centrifugation. It was subsequently washed thoroughly with deionized water and ethanol to remove any remaining impurities. The BOC-Li was then obtained as a white powder following a drying process at 60 °C for 12 h in a vacuum oven.

Characterization

X-ray diffraction (XRD) analysis was executed on a PANalytical B.V. Rayon X-ray Diffraction System to ascertain the crystal structure of the

synthesized electrocatalyst. The surface morphology was examined with precision using a Hitachi S4800 Scanning Electron Microscope (SEM) and a JEM-F200 Transmission Electron Microscope (TEM). Energy-dispersive X-ray spectroscopy (EDS) was utilized with a JED-2300T Analysis Station to evaluate the elemental composition of the samples.

X-ray photoelectron spectroscopy (XPS) was performed with a Thermo Scientific Nexsa system, powered by an Al Kα X-ray source (1486.6 eV), to obtain intricate details of the chemical composition. The C 1*s* peak, positioned at 284.8 eV, served as a reference for the calibration of binding energies. Fourier-transform infrared spectroscopy (FTIR) analysis was conducted using a Thermo Fisher Nicolet iS50, while in situ FTIR measurements were captured with a Nicolet iS50 MCT A Detector. Ultraviolet-visible (UV–Vis) spectroscopy was carried out with a UV 3600I plus instrument. Inductively coupled plasma mass spectrometry (ICP-MS) utilizing an Agilent 7700 system was employed for a comprehensive evaluation of trace Li elements.

In situ ATR-SEIRAS measurements were performed in an external reflection configuration using a custom-built accessory coupled to an FTIR spectrometer (PerkinElmer Spectrum 100 detector). Spectra were collected as an average of 16 scans with a spectral resolution of 8 cm^{-1}. A thin gold film (~10 nm) was deposited onto a silicon prism via electroless deposition. The catalyst ink was deposited onto the Au film by drop-casting 25 μL of the ink twice, allowing it to air-dry after each deposition. The catalyst-coated Si prism served as the working electrode in a three-electrode spectroelectrochemical cell, with a platinum wire as the counter electrode and an Ag/AgCl electrode (3.5 M KCl) as the reference. The cell was filled with CO_2-saturated 0.5 M $KHCO_3$ electrolyte prior to each experiment. Electrochemical control was maintained using a CHI 760E/ CHI 660E potentiostat.

Solid state Magic Angle Spinning Nuclear Magnetic Resonance (MAS NMR) experiments of the ^{7}Li state in BOC-Li sample were conducted on a Bruker 600 MHz AVANCE III operating at larmor frequency of 600.18 MHz for ^{1}H and 233.25 MHz for ^{7}Li. Instrument was equipped with H/X DVT MAS probe, supporting MAS rotor with 4.0 mm outer diameter. All the experiments conducted on Bruker 600 MHz AVANCE III were with MAS frequency of 8 kHz. Besides, we have supplemented the ^{7}Li NMR at different spinning rate (8 k, 15 k and 20 kHz) on Bruker AVANCE NEO 400 WB spectrometer operating at 155.55 MHz for ^{7}Li, equipped with 3.2 mm double-resonance MAS probe.

Operando ^{1}H, ^{17}O and ^{13}C NMR experiments were carried out on the Varian 700 MHz with an Agilent 5-mm *z*-axis pulsed-field gradient BB5 resonance probe at a ^{1}H Larmor frequency of 699.79 MHz and ^{17}O Larmor frequency of 94.87 MHz and ^{13}C Larmor frequency of 175.96 MHz. Operando ^{1}H NMR spectra were acquired using the s2pul selective excitation pulse sequence. Operando ^{17}O NMR spectra were acquired using the s2pul pulse sequence with proton decoupling. Operando ^{13}C NMR Spectra were acquired using the s2pul selective excitation pulse sequence with composite pulse ^{1}H decoupling.

Quantitative analysis of the liquid-phase products ^{2}H, ^{17}O and ^{13}C spectra and $^{13}CO_2$ adsorption experiments were acquired on Bruker AVANCE III HD 500 MHz spectrometer with a 5 mm broadband probe at a ^{1}H Larmor frequency of 500.17 MHz, ^{2}H Larmor frequency of 76.78 MHz and ^{13}C Larmor frequency of 125.77 MHz. The NMR experiments were conducted at 298 K.

Products quantification

The reaction products were analyzed using a combination of online gas chromatography (GC) and offline ^{1}H NMR spectroscopy. Gaseous products generated during CO_2 electrolysis were monitored in real time with a GC system (Ruimin GC-2060), equipped with a flame ionization detector (FID) and a thermal conductivity detector (TCD). Liquid products were quantified by offline ^{1}H NMR. The Faradaic efficiency (FE) for each product was calculated using the following equation:

$$FE = F \times n \times Z/Q \times 100\% \quad (1)$$

F is Faraday constant (96,485 C mol^{-1}), *n* is the mole of product, *Z* is the quantity of transferred electrons for each product, *Q* is total transfer charge.

Electrochemical measurements

Electrochemical measurements were performed using a CHI 760E/CHI 660E potentiostat (equipped with a 10 A current booster for high current densities tests) at an ambient temperature (298 K) and pressure. The flow rate of high-purity CO_2 in our research was controlled by a mass flow controller (Alicat Scientific).

Reference electrode calibration. All applied cathode potentials values were recorded without iR compensation. All potentials in this work were referenced to the reversible hydrogen electrode (RHE) scale. To eliminate errors associated with liquid-junction potentials, the Ag/AgCl reference electrode (3.5 M KCl) was calibrated in each electrolyte used for testing. A commercial RHE electrode (Dongping Electrochemical Instrument) with exchangeable internal electrolyte was employed as the primary standard. Before each calibration, the RHE body was filled with the same electrolyte as the test solution (1 M KOH or CO_2-saturated 0.5 M $KHCO_3$) and activated in situ by applying a cathodic potential (−9 V vs. a Pt counter) to generate a stable hydrogen layer on its internal Pt catalyst. The open-circuit potential difference between the activated RHE and the Ag/AgCl reference electrode was determined via cyclic voltammetry (CV, Supplementary Fig. 7) at a scan rate of 1 mV s^{-1} using a CHI 660E electrochemical workstation. The steady-state potential was taken as the average of the two intercepts where the current crossed zero during the forward and reverse sweeps[49]. The measured offset was negative in both electrolytes, confirming that the RHE potential lies more negative than that of Ag/AgCl under the present conditions. In 1 M KOH, the average offset (E_{offset}) was −0.9894 V, giving the conversion formula E (vs. RHE) = E (vs. Ag/AgCl) − E_{offset} = E (vs. Ag/AgCl) + 0.9894 V. In CO_2-saturated 0.5 M $KHCO_3$, the E_{offset} was −0.628 V, yielding E (vs. RHE) = E (vs. Ag/AgCl) - E_{offset} = E (vs. Ag/AgCl) + 0.628 V.

The polarization curves were meticulously recorded across a potential spectrum from 0 V to −5.0 V (vs. RHE), employing a scan rate of 10 mV/s. The electrochemical active surface area (ECSA) was estimated from double-layer capacitance measurements. Cyclic voltammetry (CV) was performed at sequentially increasing scan rates (40, 80, 120, 160, and 200 mV s^{-1}) within a non-faradaic potential window of 0.551 to 0.651 V vs. RHE without iR compensation. The capacitive current density (Δj) at 0.601 V vs. RHE was calculated for each scan rate using the following formula:

$$\Delta j = (j_a - j_c)/2 \quad (2)$$

Where j_a and j_c represent the anodic and cathodic current densities of catalysts, respectively. The calculated Δj values were then plotted against the corresponding scan rates and fitted linearly. The slope of this linear fit corresponds to the double-layer capacitance (C_{dl}).

Electrochemical impedance spectroscopy (EIS) measurements were performed at a constant potential of −0.37 V over a frequency range of 100 kHz to 1 mHz with an AC amplitude of 5 mV. The Nyquist plots were analyzed using the equivalent circuit model shown in the insets of Figs. 2b and 5b, and Supplementary Figs. 41 and 50, which consists of a solution resistance (R_s) in series with a parallel combination of a constant-phase element (CPE) and a charge-transfer resistance (R_{ct}).

Electrolysis in an H cell. The working electrode was prepared by loading catalyst onto carbon paper (SCP130N). Specifically, 10 mg of catalyst and 50 μL of Nafion solution were dispersed in 1000 μL of isopropyl alcohol, followed by ultrasonication for at least 30 min to form a homogeneous ink. A total of 100 μL (50 uL on each side) of the ink was evenly applied to both sides of the carbon paper and allowed to dry naturally, resulting in a catalyst loading (The weighted catalyst loading normalized by the geometric area) of ~1 mg cm^{-2} over a fixed area of $1 \times 1\,cm^2$ on a $1 \times 2\,cm^2$ carbon paper. A platinum plate ($1.5 \times 3\,cm^2$) served as the counter electrode. A Nafion 117 proton exchange membrane ($3 \times 3\,cm^2$, 183 μm thick) was used to separate the compartments. The membrane was pretreated by first boiling in 5 wt% H_2O_2 at 80 °C for 1 h, followed by soaking in deionized water for 30 min. It was then boiled in 5 wt% H_2SO_4 at 80 °C for 1 h and finally soaked again in deionized water for 30 min before use. The electrolyte employed was 0.5 M $KHCO_3$, prepared by dissolving 50.31 g of $KHCO_3$ and diluting to 1 L with distilled water. In the electrochemical cell, 40 mL of this solution was employed as the anolyte in the anode chamber, whereas 40 mL of the CO_2-saturated electrolyte (pH = 7.27 ± 0.04, $n = 3$) was employed as the catholyte in the cathode chamber.

Electrolysis in a flow cell. A custom three-compartment flow cell was employed for the electrolysis. The compartments were separated by an anion exchange membrane (Fumasep FAB-PK-130, $3 \times 3\,cm^2$). The membrane, with a dry-state thickness of 110–150 μm, was pretreated prior to use by soaking in 0.5 M NaCl solution at 298 K for 72 h, with the solution being replaced several times during this period. The gas diffusion electrode (GDE) was fabricated by spray-coating catalyst ink onto a gas diffusion layer (GDL, Sigracet 28 BC or 600 nm Ag/PTFE), with catalyst ink containing 25 or 50 mg catalyst sprayed onto a $3 \times 6\,cm^2$ gas diffusion layer to achieve a loading of at least 1 mg cm^{-2} or 2 mg cm^{-2}, respectively. Plastic plate with a 0.5 cm^2 window and silicone gaskets was used for structuring and sealing. A treated nickel foam ($3 \times 3\,cm^2$) served as the counter electrode. Both chambers were filled with 30 mL of 1 M KOH electrolyte (pH = 13.98 ± 0.03, $n = 3$). For stability test, both chambers were filled with 1 L of 1 M KOH electrolyte. The electrolyte was prepared by dissolving 62.34 g of KOH in distilled water and diluting to a final volume of 1 L, and was circulated at a rate of 15 mL min^{-1}.

All electrolytes mentioned above were sealed and stored in sealed polypropylene bottles at room temperature (298 K), and used within 1 week. pH measurements were performed with a LeiCi PHS-25 pH meter.

Electrochemical operando NMR setup

The operando NMR experiments were conducted using a custom-designed micro-reactor integrated within a 5 mm diameter NMR tube. The setup comprised a three-electrode electrochemical cell coupled with a plastic capillary for continuous CO_2 gas delivery (Supplementary Fig. 11), where both the counter and reference electrodes are platinum wires, and CO_2 is delivered via a PTFE capillary. The working electrode was fabricated from a bundle of ~3000 carbon microfibers (individual filament diameter of 6.9 μm). A catalyst ink was prepared by dispersing 10 mg catalyst in a mixture of 500 μL isopropanol and 100 μL Nafion 117 solution, followed by ultrasonication for at least 30 min to form a homogeneous suspension. The catalyst layer was loaded onto the carbon fiber bundle via a repeated dip-coating process: the fiber bundle was immersed in the ink, withdrawn, and dried thoroughly in an oven at 60 °C, with this cycle repeated multiple times to achieve the desired loading (~3 mg cm^{-2}). A single catalyst ink batch (prepared from 10 mg of catalyst) was used to fabricate three working electrodes simultaneously. Both the counter and reference electrodes were platinum wires with diameters of 0.3 mm. CO_2 gas was introduced into the electrolyte through a PTFE capillary (inner diameter: 0.5 mm) at a controlled flow rate of 1.5 sccm, regulated and measured using a mass flow controller (Alicat Scientific). All three electrodes and the gas capillary were assembled within the 5 mm NMR tube. Before the operando experiment, the electrode was rinsed repeatedly with deuterated water and dried; this procedure ensured the complete removal of any residual protic solvent, which is crucial for obtaining a clean NMR background.

Electrolyte preparation

Electrolytes for the operando NMR experiments were freshly prepared for each use according to the following procedures:

For operando ^{17}O NMR: The electrolyte consisted of 450 μL of deuterated water (^2H_2O) and 50 μL of $H_2{}^{17}O$ (enriched water, 35-40% isotopic purity), with 25.16 mg of $KH^{13}CO_3$ added as the bicarbonate source. The total volume was 500 μL.

For operando ^{13}C NMR: The electrolyte was 500 μL of ^2H_2O with 25.16 mg of $KH^{12}CO_3$. During the experiment, $^{13}CO_2$ gas was continuously bubbled at a flow rate of 1.5 sccm to provide the ^{13}C-labeled substrate.

DFT calculations

Calculation details. All the spin-polarized calculations were conducted using Vienna Ab-initio Simulation Package (VASP)[50,51]. The DFT functional was applied at the Perdew–Burke–Ernzerhof (PBE) level. The project-augmented wave (PAW) method was used to describe the core-valence electron interactions, with the valence electronic states expanded in plane wave basis set using an energy cutoff of 450 eV[52]. The force convergence criterion was set as 0.05 eV/Å. The transition states were searched using the constrained optimization scheme. TSs were located by varying this fixed distance, which are confirmed when (i) all atomic forces on the relevant atoms vanish and (ii) the total energy is a maximum along the reaction coordinate, while being a minimum with respect to other degrees of freedom[53–55]. To well describe the reaction system, the DFT-D3 method with the van der Waals dispersion effect included was also used[56–58].

In our calculations, the modeled surface is the (161) facet, which is consistent with the experimental observations confirmed by XRD and HRTEM (Fig. 1a, b). On the (161) surface, the exposed terminations consist of four- and three-coordinated Bi atoms (Bi_{4c}/Bi_{3c}) together with four- and three-coordinated O atoms (O_{4c}/O_{3c}). The $Bi_2O_2CO_3$ (161) surface was modeled by four-layer $p(1\times2)$ periodical slabs with the volume of 15 Å (Supplementary Fig. 21). A corresponding $1 \times 1 \times 1$ k-points mesh was consistently used during the structural optimizations to ensure reliable convergence of the calculations. For the doped surface, the introduction of low-valence Li species facilitates the formation of oxygen vacancies (O_v) on the $Bi_2O_2CO_3$(161) surface. This is evidenced by the significantly reduced O_v formation energies of −0.77 eV and −0.13 eV for Li_{3c}- and Li_{4c}-doped surfaces, respectively, compared to 3.61 eV for the pristine surface (Supplementary Fig. 22). These results clearly indicate that Li doping lowers the energetic barrier for vacancy generation, thereby making the surface more defect-rich and catalytically active under realistic reaction conditions.

In this work, the key processes under investigation mainly occur at the catalyst surface, where water dissociation and subsequent reactions are governed by the local electronic structure of surface atoms. Although the electrolyte environment can influence the energetics, an explicit solvation model would require tens or even hundreds of water molecules to faithfully capture the hydrogen-bonding network, which makes the computational cost prohibitively high for our large surface models. Therefore, in this work, we adopted an implicit solvation model, which can effectively account for the screening of the aqueous environment while maintaining computational feasibility.

The adsorption energy of surface species is defined as $E_{ads}(X) = E(X/sur) - E(sur) - E(X)$, where $E(sur)$, $E(X)$ and $E(X/sur)$ are the energies of the catalysts surface, X in the gas phase and X adsorbed on the catalyst surface, respectively. The more negative $E_{ads}(X)$ is, the more strongly the species X binds to the surface.

Calculation of free energy

To ensure that the calculated energetics are comparable to realistic electrochemical interfaces, we performed energy corrections within the computational hydrogen electrode (CHE) framework. For instance, considering a representative elementary step,

$$A^* + H^* + e^- \rightarrow AH^* + H^* \quad (3)$$

the corresponding free energy change (ΔG) is evaluated as:

$$\Delta G = \Delta E + \Delta(pV) - T\Delta S + \Delta E_{ZPE} \quad (4)$$

where ΔE is the reaction energy, $\Delta(pV)$ is typically minimal before and after the reaction, and thus is not considered in this study, $T\Delta S$ is the entropy change and can be obtained from the Handbook of Chemistry and Physics, and ΔE_{ZPE} is the zero-point energy, which can be obtained through the vibrational frequency calculations. Importantly, the reaction energy ΔE is corrected relative to the applied electrode potential. Specifically, the work function (Φ) of the catalyst surface is obtained as the difference between the vacuum level (E_{vac}) and the Fermi level (E_F). The electrode potential versus the reversible hydrogen electrode (U_{RHE}) is then determined by:

$$U_{RHE} = \frac{\Phi - \Phi_{SHE}}{e} \quad (5)$$

where Φ_{SHE} is the work function of the standard hydrogen electrode (4.60 eV is adopted in this work for $Bi_2O_2CO_3$)[59–61], and e is the elementary charge. The corrected reaction energy can thus be expressed as:

$$\Delta E = \Delta E_{cal} + e(U - U_{RHE}) \quad (6)$$

where ΔE_{cal} is the raw DFT energy obtained from VASP calculations, and U is the experimentally relevant potential (−1.18 V in this work). This correction enables our free energy profiles to properly reflect the influence of the electrochemical field, thereby bridging the gap between theoretical modeling and real electrochemical conditions.

Notably, for surface reactions on the $Bi_2O_2CO_3$ surface, the free energies of intermediates include zero-point energy corrections. Since both the reactants and products remain adsorbed on the catalyst surface, the change in entropy is expected to be very small and was therefore neglected in these cases.

In contrast, for adsorption/desorption processes, and entropy of reactant/product was fully considered. However, it is challenging to directly obtain accurate entropy values for CO_2 and HCOOH using periodic DFT package (such as VASP) with explicit aqueous models. To address this, we adopted entropy values reported in the literature, specifically $S = 231.6$ J/mol/K for CO_2 and 129.0 J/mol/K for HCOOH[62], which correspond to $T\Delta S$ terms of 0.72 eV and 0.40 eV, respectively. This correction approach is commonly used in free energy calculations and has been shown to provide a reliable estimation for such systems[63–65].

Data availability

The data generated in this study are provided in the Supplementary Information/Source Data file. Key structural data used in the DFT calculations in this study are provided in Supplementary Data 1. Source data are provided with this paper.

References

1. Gao, S. et al. Partially oxidized atomic cobalt layers for carbon dioxide electroreduction to liquid fuel. *Nature* **529**, 68–71 (2016).
2. Zhang, H., Gao, J. X., Raciti, D. & Hall, A. S. Promoting Cu-catalysed CO_2 electroreduction to multicarbon products by tuning the activity of H_2O. *Nat. Catal.* **6**, 807–817 (2023).
3. Deng, W. Y. et al. Unraveling the rate-determining step of C_{2+} products during electrochemical CO reduction. *Nat. Commun.* **15**, 892 (2024).
4. Chen, C. et al. Harnessing single-atom catalysts for CO_2 electroreduction: a review of recent advances. *EES Catal.* **2**, 71–93 (2024).
5. Ren, H. J. et al. Operando proton-transfer-reaction time-of-flight mass spectrometry of carbon dioxide reduction electrocatalysis. *Nat. Catal.* **5**, 1169–1179 (2022).
6. Sun, B. et al. Unveiling pH-dependent adsorption strength of $*CO_2^-$ intermediate over high-density Sn single atom catalyst for acidic CO_2-to-HCOOH electroreduction. *Angew. Chem. Int. Ed.* **136**, e202318874 (2024).
7. Hutchison, P., Smith, L. E., Rooney, C. L., Wang, H. & Hammes-Schiffer, S. Proton-coupled electron transfer mechanisms for CO_2 reduction to methanol catalyzed by surface-immobilized cobalt phthalocyanine. *J. Am. Chem. Soc.* **146**, 20230–20240 (2024).
8. Göttle, A. J. & Koper, M. T. M. Proton-coupled electron transfer in the electrocatalysis of CO_2 reduction: prediction of sequential vs. concerted pathways using DFT. *Chem. Sci.* **8**, 458–465 (2017).
9. Dunwell, M., Luc, W., Yan, Y., Jiao, F. & Xu, B. Understanding surface-mediated electrochemical reactions: CO_2 reduction and beyond. *ACS Catal.* **8**, 8121–8129 (2018).
10. Li, T., Yang, C., Luo, J.-L. & Zheng, G. Electrolyte driven highly selective CO_2 electroreduction at low overpotentials. *ACS Catal.* **9**, 10440–10447 (2019).
11. Zhang, Y. et al. Modulation of the electronic structure of metallic bismuth catalysts by cerium doping to facilitate electrocatalytic CO_2 reduction to formate. *J. Mater. Chem. A* **12**, 7528–7535 (2024).
12. Mukhopadhyay, S. et al. Local CO_2 reservoir layer promotes rapid and selective electrochemical CO_2 reduction. *Nat. Commun.* **15**, 3397 (2024).
13. Wang, Q. et al. Modulating active center microenvironment in phthalocyanine-based covalent organic frameworks for enhanced electrocatalytic CO_2 to CH_3OH. *Adv. Mater.* **37**, 2502644 (2025).
14. Monteiro, M. C. O. et al. Absence of CO_2 electroreduction on copper, gold and silver electrodes without metal cations in solution. *Nat. Catal.* **4**, 654–662 (2021).
15. Yang, X. et al. Cation-induced interfacial hydrophobic microenvironment promotes the C-C coupling in electrochemical CO_2 reduction. *J. Am. Chem. Soc.* **146**, 5532–5542 (2024).
16. Ding, L. et al. Over 70 % faradaic efficiency for CO_2 electroreduction to ethanol enabled by potassium dopant-tuned interaction between copper sites and intermediates. *Angew. Chem. Int. Ed.* **61**, e202209268 (2022).
17. Peng, C. et al. Ampere-level CO_2-to-formate electrosynthesis using highly exposed bismuth(110) facets modified with sulfur-anchored sodium cations. *Chem* **9**, 2830–2840 (2023).
18. Shi, Y. et al. In situ reconstruction of vegetable sponge-like Bi_2O_3 for efficient CO_2 electroreduction to formate. *Mater. Chem. Front.* **6**, 1091–1097 (2022).
19. Liu, Y. et al. Molecularly distorted local structure in Bi_2CuO_4 oxide to stabilize lattice oxygen for efficient formate electrosynthesis. *Adv. Mater.* **34**, 2202568 (2022).
20. Li, P. et al. p-d orbital hybridization induced by p-block metal-doped Cu promotes the formation of C_{2+} products in ampere-level CO_2 electroreduction. *J. Am. Chem. Soc.* **145**, 4675–4682 (2023).
21. Wen, C. F. et al. Highly ethylene-selective electrocatalytic CO_2 reduction enabled by isolated Cu-S motifs in metal-organic framework-based precatalysts. *Angew. Chem. Int. Ed.* **61**, e202111700 (2021).

22. Feng, J. et al. Improving CO_2-to-C_{2+} product electroreduction efficiency via atomic lanthanide dopant-induced tensile-strained CuO_x catalysts. *J. Am. Chem. Soc.* **145**, 9857–9866 (2023).
23. Zhang, C. et al. Concentrated formic acid from CO_2 electrolysis for directly driving fuel cell. *Angew. Chem. Int. Ed.* **63**, e202317628 (2024).
24. Zhao, C. et al. In situ topotactic transformation of an interstitial alloy for CO electroreduction. *Adv. Mater.* **32**, 2002382 (2020).
25. Tong, K. et al. Structural transition and migration of incoherent twin boundary in diamond. *Nature* **626**, 79–85 (2024).
26. Liu, C. et al. Operando formation of highly efficient electrocatalysts induced by heteroatom leaching. *Nat. Commun.* **15**, 242 (2024).
27. Chen, S. Y. et al. Unveiling the proton-feeding effect in sulfur-doped Fe-N-C single-atom catalyst for enhanced CO_2 electroreduction. *Angew. Chem. Int. Ed.* **61**, e202206233 (2022).
28. Chen, X., Wang, X. & Fang, D. A review on C1s XPS-spectra for some kinds of carbon materials. *Fuller. Nanotub. Carbon Nanostruct.* **28**, 1048–1058 (2020).
29. Cai, Y. et al. A self-cleaning heterostructured membrane for efficient oil-in-water emulsion separation with stable flux. *Adv. Mater.* **32**, 2001265 (2020).
30. Wei, Z. et al. Enhanced electrochemical CO_2 reduction to formate over phosphate-modified In: water activation and active site tuning. *Angew. Chem. Int. Ed.* **63**, e202402070 (2024).
31. Zhu, J. et al. Surface passivation for highly active, selective, stable, and scalable CO_2 electroreduction. *Nat. Commun.* **14**, 4670 (2023).
32. Jiang, Z. et al. A bismuth-based zeolitic organic framework with coordination-linked metal cages for efficient electrocatalytic CO_2 reduction to HCOOH. *Angew. Chem. Int. Ed.* **62**, e202311223 (2023).
33. Chu, Y. et al. Regulating the rate-determining step of bismuth electrocatalysts by directional facet reconstruction for efficient CO_2 reduction. *Adv. Funct. Mater.* **35**, 2508387 (2025).
34. Zhao, X. et al. Interfacial engineering of In_2O_3/InN heterostructure with promoted charge transfer for highly efficient CO_2 reduction to formate. *Chem. Eng. J.* **437**, 135114 (2022).
35. Wu, J. et al. Gas-proton microenvironment modulation for enhanced CO_2-to-formate electroreduction. *Angew. Chem. Int. Ed.* **65**, e202516163 (2025).
36. Cheng, Q. et al. Unraveling the influence of oxygen vacancy concentration on electrocatalytic CO_2 reduction to formate over indium oxide catalysts. *ACS Catal.* **13**, 4021–4029 (2023).
37. Sun, B. et al. Unveiling pH-dependent adsorption strength of $*CO_2$ intermediate over high-density Sn single atom catalyst for acidic CO_2-to-HCOOH electroreduction. *Angew. Chem. Int. Ed.* **63**, e202318874 (2024).
38. Wang, C. et al. Hydrogen-bonded organic framework supporting atomic Bi-N_2O_2 sites for high-efficiency electrocatalytic CO_2 reduction. *Angew. Chem. Int. Ed.* **63**, e202404015 (2024).
39. Li, Y. et al. Enhancing local CO_2 adsorption by L-histidine incorporation for selective formate production over the wide potential window. *Angew. Chem. Int. Ed.* **62**, e202313522 (2023).
40. Moradzaman, M. & Mul, G. Infrared analysis of interfacial phenomena during electrochemical reduction of CO_2 over polycrystalline copper electrodes. *ACS Catal.* **10**, 8049–8057 (2020).
41. Zhu, S., Jiang, B., Cai, W.-B. & Shao, M. Direct observation on reaction intermediates and the role of bicarbonate anions in CO_2 electrochemical reduction reaction on Cu surfaces. *J. Am. Chem. Soc.* **139**, 15664–15667 (2017).
42. Corson, E. R. et al. In situ ATR-SEIRAS of carbon dioxide reduction at a plasmonic silver cathode. *J. Am. Chem. Soc.* **142**, 11750–11762 (2020).
43. Qi, R. et al. Engineering oxygen vacancy in support to promote activity of In_2O_3 catalyst for CO_2 electroreduction to formate. *Adv. Funct. Mater.* **35**, e10948 (2025).
44. Jiang, Y. et al. Stabilizing oxidation state of SnO_2 for highly selective CO_2 electroreduction to formate at large current densities. *ACS Catal.* **13**, 3101–3108 (2023).
45. Zhang, B. et al. Enriching metal-oxygen species and phosphate modulating of active sites for robust electrocatalytical CO_2 reduction. *Adv. Mater.* **35**, 2304379 (2023).
46. Youzeng, L. et al. Sequentially regulating potential-determining step for lowering CO_2 electroreduction overpotential over Te-doped Bi nanotips. *Angew. Chem. Int. Ed.* **63**, e202407772 (2024).
47. Xu, B. B. et al. Operando electrochemical NMR spectroscopy reveals a water-assisted formate formation mechanism. *Chem* **10**, 3114–3130 (2024).
48. Zhao, J. Y. et al. Electro-induced crystallization over amorphous indium hydroxide gels toward ampere-level current density formate electrosynthesis. *Adv. Funct. Mater.* **34**, 2316167 (2024).
49. Wei, C. et al. Recommended practices and benchmark activity for hydrogen and oxygen electrocatalysis in water splitting and fuel cells. *Adv. Mater.* **31**, 1806296 (2019).
50. Kresse, G. & Hafner, J. Norm-conserving and ultrasoft pseudopotentials for first-row and transition elements. *J. Phys. Condens. Matter* **6**, 8245–8257 (1994).
51. Kresse, G. & Furthmuller, J. Efficiency of ab-initio total energy calculations for metals and semiconductors using a plane-wave basis set. *Comput. Mater. Sci.* **6**, 15–50 (1996).
52. Kresse, G. & Joubert, D. From ultrasoft pseudopotentials to the projector augmented-wave method. *Phys. Rev. B* **59**, 1758–1775 (1999).
53. Alavi, A., Hu, P. J., Deutsch, T., Silvestrelli, P. L. & Hutter, J. CO oxidation on Pt(111): an ab initio density functional theory study. *Phys. Rev. Lett.* **80**, 3650–3653 (1998).
54. Liu, Z.-P. & Hu, P. General rules for predicting where a catalytic reaction should occur on metal surfaces: A density functional theory study of C-H and C-O bond breaking/making on flat, stepped, and kinked metal surfaces. *J. Am. Chem. Soc.* **125**, 1958–1967 (2003).
55. Wang, H. F. et al. Structural origin: Water deactivates metal oxides to CO oxidation and promotes low-temperature CO oxidation with metals. *Angew. Chem. Int. Ed.* **51**, 6657–6661 (2012).
56. Wang, H. F. et al. Unexpected C-C bond cleavage mechanism in ethylene combustion at low temperature: origin and implications. *ACS Catal.* **6**, 5393–5398 (2016).
57. Grimme, S., Ehrlich, S. & Goerigk, L. Effect of the damping function in dispersion corrected density functional theory. *J. Comput. Chem.* **32**, 1456–1465 (2011).
58. Ji, X.-X., Wang, H.-F. & Hu, P.-J. First principles study of Fenton reaction catalyzed by FeOCl: reaction mechanism and location of active site. *Rare Met.* **38**, 783–792 (2018).
59. Hu, X. et al. What is the real origin of the activity of Fe-N-C electrocatalysts in the O_2 reduction reaction? Critical roles of coordinating pyrrolic N and axially adsorbing species. *J. Am. Chem. Soc.* **144**, 18144–18152 (2022).
60. Zhao, X. & Liu, Y. Origin of selective production of hydrogen peroxide by electrochemical oxygen reduction. *J. Am. Chem. Soc.* **143**, 9423–9428 (2021).
61. Duan, Z. & Henkelman, G. Theoretical resolution of the exceptional oxygen reduction activity of Au(100) in alkaline media. *ACS Catal.* **9**, 5567–5573 (2019).
62. Lide, D. R. CRC Handbook of Chemistry and Physics (CRC Press, 2004).
63. Ren, G., Zhou, M. & Wang, H. Weakened interfacial hydrogen bond connectivity drives selective photocatalytic water oxidation toward H_2O_2 at water/brookite-TiO_2 interface. *J. Am. Chem. Soc.* **146**, 6084–6093 (2024).
64. Ren, G., Zhou, M., Hu, P., Chen, J.-F. & Wang, H. Bubble-water/catalyst triphase interface microenvironment accelerates

photocatalytic OER via optimizing semi-hydrophobic OH radical. *Nat. Commun.* **15**, 2346 (2024).
65. Zhou, M. & Wang, H. Optimally selecting photo- and electro-catalysis to facilitate CH_4 activation on TiO_2(110) surface: localized photoexcitation versus global electric-field polarization. *JACS Au* **2**, 188–196 (2021).

Acknowledgements

This project was supported by Shanghai Municipal Science and Technology Commission(Grant No.YDZX20243100003001001), National Key Research and Development Program of China (2021YFA1500700), the National Natural Science Foundation of China (grant nos. 22572052, 22274052, 22072045, and 21574043), the Science and Technology Commission of Shanghai Municipality (25ZR1402129 and 25DZ3000302), the International (Regional) Cooperation and Exchange Projects of the National Natural Science Foundation of China (51920105003), the Science and Technology Commission of Shanghai Municipality (21DZ1207101), and the Microscale Magnetic Resonance Platform of ECNU.

Author contributions

X.-L.W. conceived and designed the project. Y.S. conducted experimental work, while Y.L. carried out computational simulations. H.D., G.F., and H.Z. assisted with NMR experimentation and data analysis. Results were collaboratively analyzed by Y.S., Y.L., X.-L.W., H.W., and Y.-F.Y. The manuscript was drafted by Y.S., Y.L., X.-L.W., H.W., and Y.-F.Y., with critical revisions from all authors.

Competing interests

The authors declare no competing interests.

Additional information

Supplementary information The online version contains supplementary material available at https://doi.org/10.1038/s41467-026-68604-z.

Correspondence and requests for materials should be addressed to Haifeng Wang, Xue-Lu Wang or Ye-Feng Yao.

Peer review information *Nature Communications* thanks the anonymous reviewer(s) for their contribution to the peer review of this work. A peer review file is available.